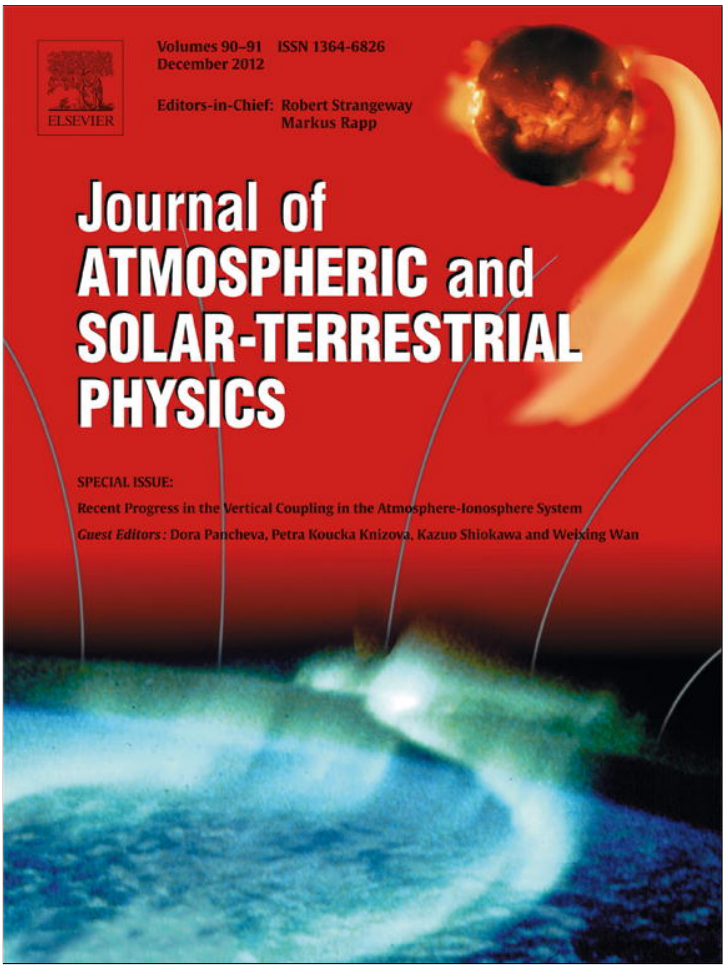

Journal of Atmospheric and Solar-Terrestrial Physics 90–91 (2012) 117–123

Contents lists available at SciVerse ScienceDirect

Journal of Atmospheric and Solar-Terrestrial Physics

journal homepage: www.elsevier.com/locate/jastp

Forward ray-tracing for medium-scale gravity waves observed during the COPEX campaign

I. Paulino [a,*], H. Takahashi [a], S.L. Vadas [b], C.M. Wrasse [c], J.H.A. Sobral [a], A.F. Medeiros [d], R.A. Buriti [d], D. Gobbi [a]

[a] Instituto Nacional de Pesquisas Espaciais, São José dos Campos, SP, Brazil
[b] Colorado Research Associates, Boulder, CO, USA
[c] Vale Soluções em Energia, São José dos Campos, SP, Brazil
[d] Universidade Federal de Campina Grande, Campina Grande, PB, Brazil

ARTICLE INFO

Article history:
Received 3 November 2011
Received in revised form
1 June 2012
Accepted 9 August 2012
Available online 21 August 2012

Keywords:
Airglow
Gravity wave
Plasma bubble
Ray-tracing

ABSTRACT

Medium-scale gravity waves (MSGWs) observed during the Conjugate Point Experiment (COPEX) at Boa Vista (2.8°N; 60.7°S, dip angle 21.7°) have been ray-traced and studied based on zero wind and model wind conditions. Wind profiles have been used from the TIE-GCM and HWM-07 models. Temperature profiles were used from the NRLMSISE-00 and TIE-GCM models, and TIMED/SABER satellite data. Doppler up-shifted MSGWs, at ~87 km of altitude, propagated to higher altitudes into the thermosphere–ionosphere domain than waves that were un-shifted. Most MSGWs propagated upwards up to ~140 km of altitude and were seen to be unlikely candidates to trigger equatorial plasma bubbles (EPBs) at the F layer bottom side. However, three of them propagated up to heights close to the F layer bottom side, where it could act in the EPB seeding directly. Moreover, three MSGWs, which propagated equatorward, could act on EPB seeding by field-line-integrated effects.

1. Introduction

Depending on the local thermodynamic condition, atmospheric gravity waves (GWs) can be refracted, reflected or absorbed in the ambient atmosphere. These last two physical processes are responsible for filtering a GW spectrum when it propagates upward from the lower to middle and upper atmosphere. Critical level (where a GW is absorbed) and turning level (where a GW is reflected) filtering are a result of the vertical variations in the wind and temperature profiles. So, if a GW escapes from these levels, it can potentially propagate to high altitudes in the thermosphere–ionosphere (TI). However, above ~100 km, molecular viscosity and thermal diffusivity increase considerably with altitude (due to the decreasing background atmospheric density).

Depending on its vertical wavelength and intrinsic period, a gravity wave's amplitude increases nearly exponentially with altitude until it succumbs to dissipative processes. At that point, it completely dissipates and the amplitude becomes ~0. Hence, all the energy and momentum are transferred into the background atmosphere. These GW breaking processes modify the properties of the thermosphere background (Miyoshi and Fujiwara, 2008; Yigit et al., 2009; Vadas and Nicolls, 2009; Vadas and Liu, 2009, 2011; Yigit and Medvedev, 2010).

In the last few decades, many authors have considered gravity waves as a possible mechanism for seeding of equatorial plasma bubbles (EPBs). Indeed, theoretical (e.g., Richmond, 1978; Anderson et al., 1982; Huang et al., 1993; Huang and Kelley, 1996; Sultan, 1996; Tsunoda, 2007, 2010; Keskinen and Vadas, 2009; Kherani et al., 2009) and observational (e.g., Kelley et al., 1981; Sobral et al., 1981, 2001; Rottger, 1982; Hysell et al., 1990; McClure et al., 1998; Vadas and Nicolls, 2008; Takahashi et al., 2010, 2011) studies have provided significant process in this concern. However, about the sources of these GWs, it is still an open question. Gravity waves could be generated either in the troposphere by convective plumes and propagate into the lower TI (e.g., Pfister et al., 1993; Dewan et al., 1998; Taylor et al., 1998; Sentman et al., 2003; Suzuki et al., 2007) or by wind shear or thermospheric body forcing in the thermosphere (e.g., Fritts and Alexander, 2003; Vadas and Fritts, 2009; Vadas and Liu, 2011).

Recent measurements from the SpreadFEx campaign (Fritts et al., 2009), conducted at several Brazilian equatorial sites in 2005, revealed important new aspects about the seeding of EPB by the waves from lower altitudes. Kherani et al. (2009) simulated two gravity waves occurring during the SpreadFEx, and examined propagations of them from a convective source region. They concluded that GWs may play an important role in the EPB seeding depending on the ionospheric conditions. Using the Rayleigh–Taylor instability (RTI) linear theory, Abdu et al. (2009a) studied the effects of GWs observed by ionosonde data on. They concluded that a large GW induced winds could contribute for a fast growth of the

* Corresponding author. Tel.: +55 12 3208 7167; fax: +55 12 3208 6990.
E-mail address: igo@dae.inpe.br (I. Paulino).

1364-6826/$ - see front matter © 2012 Elsevier Ltd. All rights reserved.
http://dx.doi.org/10.1016/j.jastp.2012.08.006

polarization electric filed, and, consequently, causing more efficient development of spread-F. Another important result from the SpreadFEx campaign was find an evidence of gravity waves at the bottom of the F layer originating from the tropospheric deep convection system (Vadas et al., 2009). Fritts et al. (2008) argued the existence of large GW amplitudes in the wind and temperature at these heights. They showed that gravity waves modulated by tides, for example, enhance their parameters and influence the plasma instability growth rates. Finally, a linear relationship between EPB spacing and wavelength of medium-scale gravity waves (MSGWs) observed at the OH layer ($\sim$87 km height) was presented and discussed by Takahashi et al. (2009) as an evidence of neutral–ion atmosphere coupling.

Makela et al. (2010) observed periodic EPB spacing structure at La Serena in Chile (29.9°S), and mentioned that the spacing was comparable to the secondary GW spectrum (manifested as traveling ionospheric disturbances—TIDs) generated from deep convections. During the COPEX campaign carried out at Boa Vista (2.8°N; 60.7°S, dip angle 21.7°N) in November and December 2002, plasma bubble observation by an OI630 nm airglow imager indicated an almost linear relationship between the horizontal wavelength of MSGWs and the EPB spacing (Paulino et al., 2011). These studies strengthen the hypothesis that gravity waves could have an important role for the initial development of equatorial spread-F. Some studies have pointed out that the eastward thermospheric wind is the primary controlling factor for the initiation of the irregularities (Kudeki and Bhattacharyya, 1999; Kudeki et al., 2007). In this case, gravity waves will not be necessarily required to trigger the RTI. However, in this case, it would be necessary to have appropriate ionospheric conditions for the EPB development.

The present work is a continuation of the studies of MSGWs and EPBs observed at Boa Vista during the COPEX campaign (Abdu et al., 2009b; Sobral et al., 2009; Paulino et al., 2011). We simulated the propagation of GWs into the TI using the ray-trace methodology by Vadas and Fritts (2005) and Vadas (2007) in order to investigate the growth of their amplitudes in the wind fields. Results from the ray-tracing will improve our understanding of the role that GWs have in EPB seeding in the F layer bottom side. Evaluation of the wind effect on the GW propagation is discussed here in two cases: zero wind (ZW) and model wind (MW) conditions. Ray-tracing temperature database was employed from the TIMED/SABER satellite and numerical models, and wind profiles were taken from models. Details about ray-tracing database are presented in Section 2. Results are in Section 3, and discussed in Section 4.

2. Ray-tracing methodology and database

Medium-scale gravity waves observed during the COPEX campaign were ray-traced based on the model of Vadas and Fritts (2005). In this model, GW dissipation due to molecular viscosity and thermal diffusivity were included in order to consider the damping of high-frequency GW in the TI. The GW dispersion relation for non-hydrostatic and compressible fluids is used, but it excludes acoustic waves similar to Marks and Eckermann (1995). It can be written as

$$\omega_{Ir}^2+\frac{v^2}{4}\left(\mathbf{k}^2-\frac{1}{4H^2}\right)^2\left(1-\frac{1}{Pr}\right)^2\frac{\left(1+\delta_+ +\frac{\delta^2}{Pr}\right)}{\left(1+\frac{\delta_+}{2}\right)^2}+\frac{v_+ m\omega_{Ir}}{H}+\frac{v^2m^2}{PrH^2}=\frac{k_H^2N^2}{\mathbf{k}^2+\frac{1}{4H^2}}, \quad (1)$$

where ω_{Ir} is the real part of the intrinsic frequency, v is the molecular viscosity, $\mathbf{k}^2=k^2+l^2+m^2$, and (k,l,m) is the wavenumber vector, Pr is the Prandtl number (in this work, it was used Pr=0.7), $\delta=vm/H\omega_{Ir}$, $\delta_+=\delta(1+Pr^{-1})$, $v_+=v(1+Pr^{-1})$, $H=-\overline{\rho}(d\overline{\rho}/dz)$ is the scale height, $\overline{\rho}$ is the mean density, $N=\sqrt{(g/\overline{\theta})d\overline{\theta}/dz}$ is the buoyancy frequency, g is the gravitational acceleration, $\overline{\theta}=\overline{T}(p_o/\overline{p})^{R/C_p}$ is the potential temperature, $\overline{T}$ and $\overline{p}$ are the mean temperature and pressure, respectively, $R=8314.5/X_{MW}$ is the gas constant, $C_p=\gamma R/(\gamma-1)$ is the mean specific heats at constant pressure, $\gamma=C_p/C_v$, C_v is the mean specific heats at constant volume, and X_{MW} is the mean molecular weight of the particle in the gas. More details how to calculate these variables can be found in Vadas (2007). On the other hand, the imaginary part of the intrinsic frequency gives the inverse decay rate in the time for a dissipating GW and can be written as

$$\omega_{Ii}=-\frac{v}{2}\left(\mathbf{k}^2-\frac{1}{4H^2}\right)\frac{1+(1+2\delta)/Pr}{1+\delta_+/2}. \quad (2)$$

Since ω_{Ii} changes in time and space, the spectral momentum flux per unit mass when a GW is launched from $z=z_i$ and $t=t_i$ (Vadas and Fritts, 2009, Eq. 50) is

$$\tilde{u_H}\tilde{w}^*(\vec{x},t)=\left|\overline{\tilde{u_H}\tilde{w}^*}\right|_{t_i}\frac{\overline{\rho(z_i)}}{\overline{\rho(z)}}e^{-2\int_{t_i}^{t}|\omega_{Ii}|\,dt'}, \quad (3)$$

where $\vec{x}=(x_1,x_2,x_3)=(x,y,z)$ is the position of the wave at each time t, $\tilde{u_H}$, and $\tilde{w}$ are the horizontal and vertical winds due to the GW, and $*$ means the complex conjugate.

The Vadas and Fritts (2005) ray-tracing model follows the formalism of Lighthill (1978), i.e., the wind, density and other background parameters are assumed to change slowly with altitude. If a wave packet is propagating in a background wind $\vec{V}(\vec{x})=(V_1,V_2,V_3)=(u,v,w)$, then its evolution can be described by

$$\frac{dx_i}{dt}=V_i+\frac{\partial\omega_{Ir}}{\partial k_i}=V_i+c_{g_i} \quad (4)$$

and

$$\frac{dk_i}{dt}=-k_j\frac{\partial V_j}{\partial x_i}-\frac{\partial\omega_{Ir}}{\partial x_i}, \quad (5)$$

where $\omega_{Ir}=\omega_{Or}-ku-lv$, ω_{Or} is the observed frequency of each GW, $i,j=1,2,3$ and repeated indices imply a summation. Using the ray-tracing results and the model described by Vadas and Fritts (2009) it is possible to reconstruct the gravity wave fields (temperature, density, zonal, meridional, and vertical wind velocities) from GW sources (such as a deep convection plume).

In the present work, the initial position has been assumed to be equal to the location of the observatory and the OH airglow layer, i.e., $\vec{x_i}=(x_i,y_i,z_i)=(36.4°\text{W},7.5°\text{S},87\text{ km})$. The initial wave vector was taken from the OH images (horizontal component, $k_i=2\pi/\lambda_{x_i}, l_i=2\pi/\lambda_{y_i}$, where $\lambda_H^2=\lambda_{x_i}^2+\lambda_{y_i}^2$) and from the dispersion relation (vertical component) shown in Eq. (1). The initial intrinsic frequency was calculated by $\omega_{Ir}=(2\pi/\tau_i)-kU-lV$, where τ_i is the observed period.

Each GW's amplitude was inferred from the fractional intensity perturbation in the images $(I'/\overline{I})$. Then, the cancelation factor (CF) equation of the Vargas et al. (2009) has been used to calculate the fractional temperature perturbation as $(T'/\overline{T})=(I'/\overline{I})/CF$. Following the methodology described by Vadas et al. (2009), the average momentum flux, at the OH layer, was estimated for all waves. In addition, the reconstruction of the gravity wave fields ($\tilde{u}$, $\tilde{w}$, $\tilde{T}$, $\tilde{\rho}$), for a specific height were calculated as the same form of Vadas and Fritts (2009).

The ray tracing starts at the OH height and goes downward until to touch the ground. After, it goes upward until the GW

dissipates completely. The algorithm excludes GWs with group speed higher than 90% of the sound speed. The ray tracing stops whenever either the local kinematic viscosity varies quickly or the GW reaches a critical level.

The biggest challenge in the use of the ray-trace methodology for GW studies is to obtain temperature and wind profiles from the surface to TI heights. In the present work, we use the daily mean temperature measured by the TIMED/SABER satellite over Boa Vista area ($20^\circ \times 20^\circ$). Fig. 1 illustrates a mean daily temperature profile on 5–6 October 2002. In this case, 12 profiles were used to yield the mean profile. Fig. 1(a) shows the position and time of the satellite measurements near Boa Vista. Two satellite orbits passed over the Boa Vista area, the first one between $\sim 10:48$ and 11:08 UT on 5 October 2002, and another one from 02:10 to 02:28 UT on 6 October 2002. The corresponding profiles are plotted as dashed lines in Fig. 1(b). The heavy line represents the mean temperature profile and the error bars represent standard deviation.

No other temperature nor wind measurements from the ground were made during the COPEX campaign. Therefore, temperature profiles were supplemented by the NRLMSISE-00 (Picone et al., 2002) from the surface to 20 km height, and by the Thermosphere–Ionosphere-Electrodynamic General Circulation Model (TIE-GCM, Roble and Ridley, 1994) above 130 km. Wind

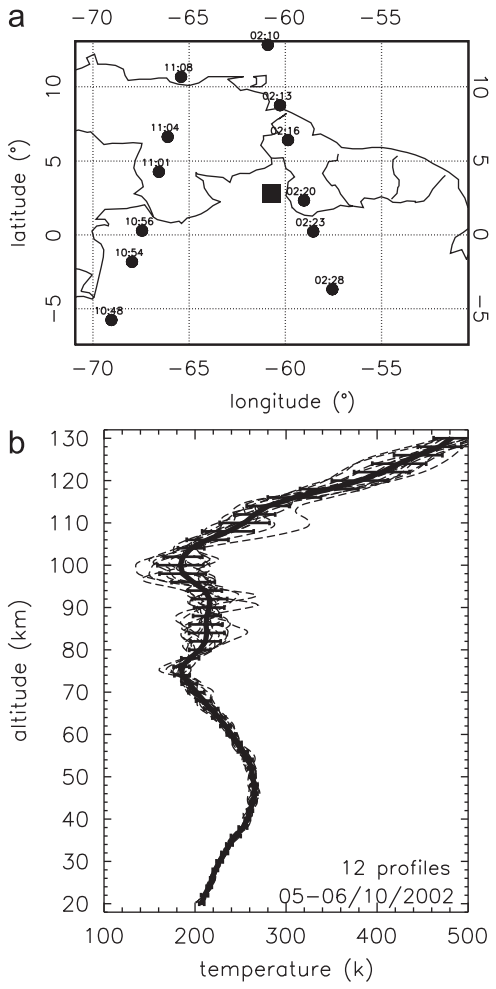

Fig. 1. Temperature profiles measured by the TIMED/SABER satellite. (a) Filled circles indicate the position of each sounding of the satellite on the geographic map on 02–06 October 2002, close to Boa Vista (filled square). Universal Time of the measurements are printed above the respective circles. (b) Averaged mean temperature profile on this day is shown by heavy line. Error bars are the standard deviation of the mean. Twelve profiles were plotted as dashed lines.

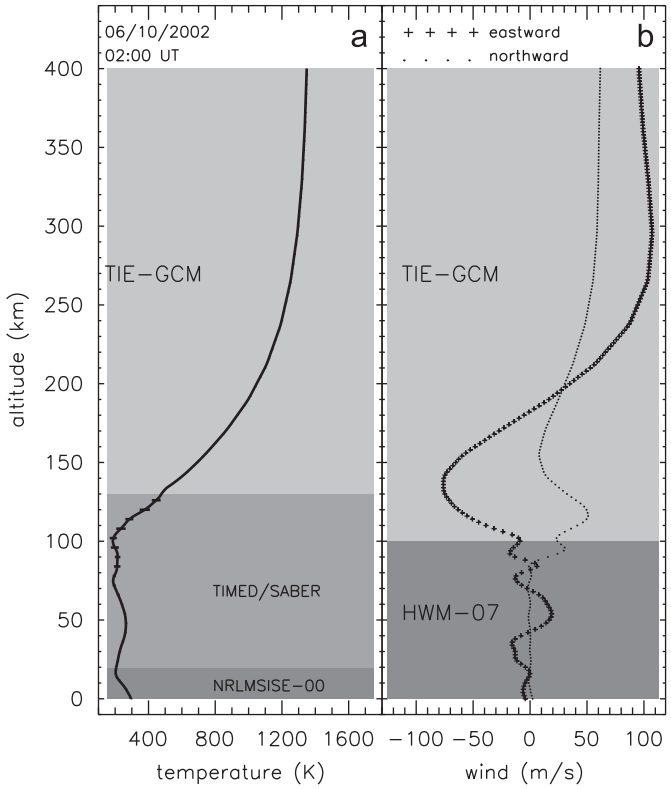

Fig. 2. Mean temperature and wind profiles at 02:00 UT on 6 October 2002. Shaded areas indicate the range chosen for each model/measurement labeled in the respective box. (a) Temperature profile. From the ground to 20 km height was used the NRLMSISE-00 model. Between 20 and 130 km is shown a daily temperature from the SABER. Above 130 km, TIE-GCM was plotted. (b) '+++' is to the eastward wind profile and '…' is to northward one. HWM-93 was used below 100 km and TIE-GCM above it.

profiles were built from the TIE-GCM model above 100 km and the Horizontal Wind Model (HWM07 Drob et al., 2008) from the ground to 100 km. Vertical wind was assumed to be zero in the whole atmosphere. Fig. 2 shows temperature and wind profiles (plus and dot symbols representing eastward and northward, respectively) from the surface to 400 km of altitude at 02:00 UT on 6 October 2002. Shaded areas indicate each model/measurement range used for all the profiles. For ray-tracing, there are temperature and wind profiles every 2 h and every 2 km in altitude from the ground to 400 km. These parameters are assumed to be latitude and longitude independent. SABER temperature profiles used (from 20 to 130 km) were obtained by taking an average of all the observed profiles of the day in concern.

3. Results

All MSGWs observed during the COPEX campaign (Paulino et al., 2011) were ray-traced using two different wind conditions: (1) zero wind (ZW) and (2) model wind (MW). Ray-tracing each MSGW through both zero and model winds allow us to investigate the role of the wind in altering the predicted ray path of the GWs. As we are interested in investigating possible GW effect in TI dynamics, the present work will focus on the forward ray-trace results.

Fig. 3 shows the forward horizontal paths of the MSGWs plotted on a geographic map for (a) zero wind (ZW) and (b) model wind (MW). 'Plus' symbols represent the position of the maximum momentum flux for each MSGW. 'Star' symbols

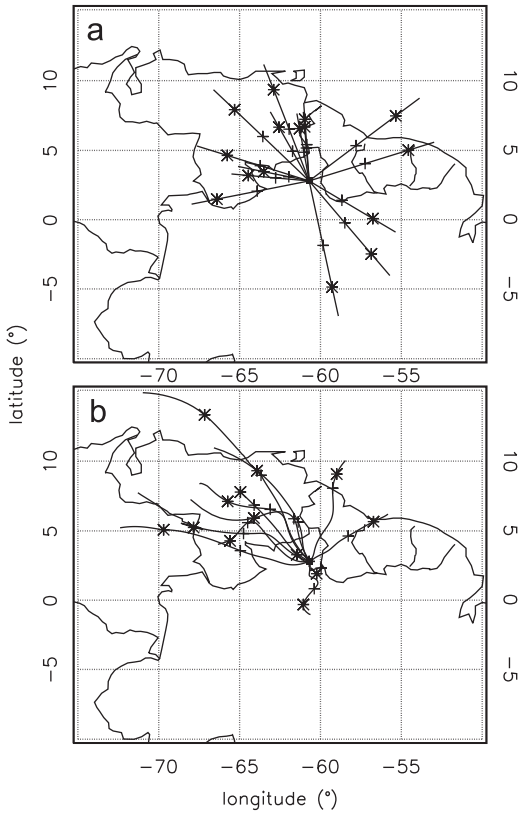

Fig. 3. Horizontal ray path for the 15 MSGWs observed during the COPEX campaign. (a) is to zero wind and (b) is to wind from the model/measurements. '+' represents where the momentum flux is maximum and '*' represents the position where the momentum flux is less than 1% of the initial momentum flux at 87 km height.

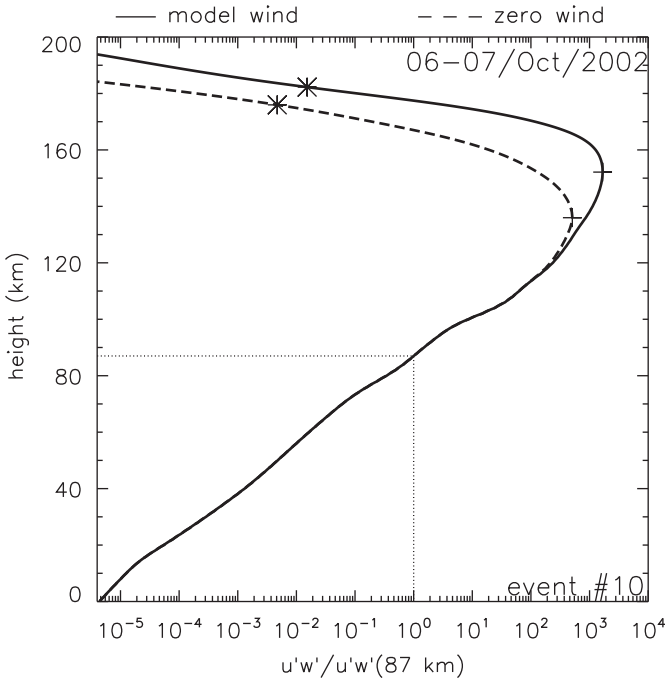

Fig. 4. Relative momentum flux $\overline{u'w'}(z)/\overline{u'w'}(87\text{ km})$ for the model (solid line) and zero (dashed line) winds on 06–07 October 2002. '+' is the height of dissipation, that is, the altitude where the momentum flux is the maximum. '*' is the height where the momentum flux is less than 1% of the momentum flux at 87 km.

indicate the position where the momentum flux was less than 1% of the initial value (at 87 km) for each GW.

The position and time of the maximum momentum flux occurs prior the GW starts the dissipation (e.g., Vadas, 2007; Vadas et al., 2009). This is a critical position/time where the wave has the largest momentum. Above/after this level, the wave amplitude diminishes rapidly. When the wave momentum flux decays to less than 1% of its initial value, it is totally dissipated.

The definition of position/time prior to dissipation is clear in Fig. 4. For this MSGW #10 (MSGWs were numbered in Tables 1 and 2), the height prior to dissipation was higher for the model wind case (solid line) than for the zero wind case (dashed line), although the momentum flux profiles were similar below 130 km.

Comparing the two cases, ZW with MW, shown in Fig. 3, it can be seen that the positions of maximum momentum flux ('plus') due to ZW and MW are not significantly different. That is, the MW did not significantly affect the propagation of the MSGWs in the lower thermosphere (<125 km). However, above the maximum momentum flux heights, the GW paths with the MW are westward tilting for almost all of them. This GW spectrum could propagate horizontally from Boa Vista to 150–530 km away for the ZW condition, and up to 590 km for the MW condition, prior to its dissipation.

Up to attaining less than 1% of their initial momentum flux, the GW horizontal propagations are confined between 300–780 km for the ZW condition and 100–1200 km for the MW condition. Details about the MSGWs at maximum momentum flux and 1% of the initial momentum flux are shown in Tables 1 and 2, respectively (event numerations are the same as presented in Table 1 by Paulino et al., 2011). In most of the cases, the MSGWs propagated

Table 1
Ray-tracing results for the maximum momentum flux. 'ZW' is to zero wind and 'MW' is to model wind. Shift column shows 'dn' down-shifted GW due to the wind and 'up' up-shifted GW.

Event #	Horizontal distance (km)		Height (km)		Travel time (h)		u'_H (m/s)		u'_m (m/s)		Shift
	ZW	MW	ZW	MW	ZW	MW	ZW	MW	ZW	MW	
1	231.5	523.1	113.4	102.1	1.9	5.3	12.5	10.7	11.9	10.2	up
2	427.8	607.1	114.0	131.4	2.6	3.6	30.1	20.3	27.0	18.1	up
3	366.1	479.7	118.0	108.2	2.0	2.4	10.7	10.9	10.7	10.9	dn
4	436.8	761.6	118.0	110.8	2.2	2.6	20.8	22.2	2.0	2.4	dn
5	273.6	98.0	99.5	137.1	4.9	2.7	10.2	11.4	6.7	7.6	up
6	416.6	221.9	106.0	133.9	4.3	2.7	14.5	15.8	5.4	6.2	up
7	263.3	494.2	114.0	108.9	1.9	4.0	17.9	15.5	4.0	3.6	dn
8	356.5	502.0	110.8	105.1	2.9	4.2	15.7	16.5	13.4	14.2	dn
9	264.5	324.3	128.0	106.1	1.3	1.4	15.0	23.2	2.4	3.5	dn
10	408.3	336.6	136.0	152.1	1.3	1.1	20.4	19.3	20.3	19.0	up
11	476.3	586.4	129.4	112.0	1.9	1.9	14.0	21.3	7.0	10.6	dn
12	143.6	–	96.8	–	3.7	–	18.9	–	17.0	–	dn
13	232.5	357.6	118.0	104.0	1.4	2.5	22.1	23.0	1.6	1.4	dn
14	526.7	–	126.1	–	2.1	–	18.5	–	0.9	–	dn
15	291.5	–	131.1	–	1.2	–	16.2	–	2.8	–	dn

far from Boa Vista when the model wind was used instead of the zero wind.

All the dissipation heights (i.e., the altitude of maximum momentum flux) are located between 96 and 136 km for the zero wind (4th column of Table 1) and between 102 and 153 km for the model wind (5th column of Table 1). Note that the dissipation heights are similar for both the cases, indicating little change in this altitude from the background wind. The travel time of the gravity wave prior to dissipation is between 1 and 5.3 h for both wind conditions.

Horizontal GW amplitudes were calculated, following the Vadas and Fritts (2009) methodology, and shown in Table 1

Table 2
Similar to Table 1, but for the momentum flux less than 1% of the initial momentum flux (87 km).

Event #	Horizontal distance (km)		Height (km)		Travel time (h)		Shift
	ZW	MW	ZW	MW	ZW	MW	
1	418.5	543.9	132.2	104.0	3.5	7.4	up
2	785.5	689.9	133.5	143.2	5.0	4.3	up
3	637.2	901.6	139.3	113.6	3.6	4.1	dn
4	753.7	1195.0	138.3	115.3	3.9	3.8	dn
5	532.0	104.9	109.0	154.5	9.6	3.1	up
6	725.5	310.2	116.4	150.1	7.6	3.3	up
7	476.7	689.4	132.9	115.5	3.5	5.7	dn
8	569.8	924.9	122.4	112.9	4.9	6.0	dn
9	429.2	734.0	152.7	113.3	2.2	2.9	dn
10	711.5	469.8	173.0	173.8	2.3	1.5	up
11	755.1	725.9	151.7	115.2	3.1	2.1	dn
12	320.3	–	102.1	–	8.0	–	dn
13	416.9	480.0	142.4	108.0	2.6	4.9	dn
14	848.4	–	148.1	–	3.5	–	dn
15	480.8	–	161.2	–	2.1	–	dn

(columns 8th and 9th). It is important to note that the gravity wave winds prior to dissipation were significant, i.e., larger than 10 m/s for all of them and reached $\sim$30 m/s (event #2 for ZW condition). Columns 10th and 11th of Table 1 show the GW induced zonal winds (in geomagnetic coordinates). When the gravity wave propagation direction is almost parallel to the geomagnetic equator, the zonal wind is very close to the total horizontal wind (e.g., events #1–3, #8, and #10).

The last columns of Tables 1 and 2 show the gravity wave Doppler shift at the OH layer altitude, 'up' and 'dn' meaning up-shifted and down-shifted, respectively. Almost all up-shifted GWs propagate higher than un-shifted GWs, only the event #1 does not follow this rule. Finally, Table 2 complements the results of Table 1, for instance, most of the MSGWs traveled few hours (<5) and reached $\sim$135 km height until attaining less than 1% of their initial momentum flux. Up-shifted MSGWs also propagated to the highest altitudes, except the event #1.

The cases without number in Tables 1 and 2 indicate that the corresponding MSGW does not reach at the maximum momentum flux point due to action of critical levels. The presence of these critical levels was the primary difference when it was compared the ray-tracing results using the HWM-93 (Hedin et al., 1996) and HWM-07 models.

4. Discussion and conclusion

TIE-GCM neutral temperature profiles present a coherent daily variability that show an increase during the local afternoon and a cooling after midnight. Moreover, the exospheric temperature changes according to the solar cycle, that is, the thermospheric temperatures increase (decrease) with the increase (decrease) of solar activity. The MSGW measurements at Boa Vista were carried out in 2002, during the period of high solar activity. Regarding the wind profiles, between 120 and 220 km of altitude the zonal wind is normally westward during the evening period, and above 220 km it is eastward. However, the winds could be variable from day to day with any other dynamical processes.

Comparing Fig. 3(a) and (b), it can be seen that the thermospheric winds alter the wave trajectory, especially for the east and west directions (note that the eastward wind is higher than northward). However, the difference in height of the maximum momentum flux for with and without wind is small. The path modification in the horizontal path due to the wind was primary a consequence of a northwestward wind between 100 and 180 km during the nighttime. In this case, the wind acts as breaking the waves, and can also change the direction of the GW propagation (events #2, #5, and #6) a little.

When a GW propagates in the atmosphere, the background winds change the frequency, i.e., $\omega_{Ir}=\omega_{Or}-ku-lv$. Thus, depending on the wind intensity and direction, a GW can be down-shifted (up-shifted) and the intrinsic frequency decreased (increased). Down-shifted GWs dissipate at lower altitudes, while up-shifted GWs tend to dissipate at higher altitudes with larger amplitude and momentum flux, as shown theoretically by Fritts and Vadas (2008) and Fritts et al. (2008). It happens because increasing the intrinsic frequency, the GWs can easily escape from the absorption process by critical levels.

From Tables 1 and 2, it can be seen that when the wave frequency was upward shifted in the MLT region (where our ray-tracing starts), it propagates much higher and, in some cases, the amplitude is larger as well. If the wave frequency was downward shifted, it propagates to a lower altitude, and loses momentum much faster than the case of upward shifted GW. Therefore, it seems that the wind structure in the MLT region may play an important role for the condition of the upward propagation of GWs. The current results are in agreement with the theoretical predictions by Fritts et al. (2008). This result depends on our use of the TIE-GCM in the thermosphere, which does not include some important lower atmospheric components to the wind. Therefore, we cannot rule out cases when the thermospheric wind changes its direction drastically and cause Doppler down-shift in TI.

Besides a GW reaching high altitudes in the TI, its phase propagation direction is very important for influencing the spread-F generation by the RTI mechanism. Fritts et al. (2008) showed that GWs propagating westward are likely a more effective contributor for triggering the RTI in the F layer bottom side. In the present work, columns 10 (u'_m, ZW) and 11 (u'_m, MW) of Table 1, there are cases of gravity waves propagating almost parallel to the magnetic equator with large zonal wind amplitudes. Moreover, the events #2 and #10 presented the largest zonal wind amplitude, respectively, 27 and 20 m/s for the ZW condition, and 18 and 19 m/s for the MW condition.

Fig. 5 shows the complete ray path of the event #10: Fig. 5(a) depicts the vertical trajectory as a function of the time, and Fig. 5(b) shows the horizontal trajectory on the map. The parameters of the MSGW are also shown in this figure. The GW propagated almost parallel to $\sim 20^\circ$ magnetic latitude. Furthermore, the dissipation of the GW happened at high altitudes (above $\sim$150 km) and extended up to the bottom side of F region (180–200 km) as can be seen in Fig. 5(a). In this case we expect a favorable condition for EPB with a spacing of the GW horizontal wavelength ($\sim$190 km). Unfortunately, no EPB spacing close to this GW wavelength were observed in this evening. It could be because the EPB generated by this GW occurred far east of the imager observation area, and therefore was not possible to observe from Boa Vista. Investigating gravity wave effects in the TI using an airglow imager would be more efficient for GWs propagating westward. Although the present observations show few GWs propagating westward, the TIE-GCM wind during the nighttime, in the lower thermosphere, is primary westward, and acts impeding them to attain high altitudes.

Takahashi et al. (2009) and Paulino et al. (2011) showed a quasi-linear relationship between EPB spacing and horizontal wavelength of MSGWs. Makela et al. (2010) presented a direct correlation between these parameters as well. The present ray-tracing results may give a new vision about these physical relationships. GWs could influence RTI seeding in two ways: (1) propagating directly to the bottom side of the F layer ($\sim$ 200–250 km) at the equatorial region, and (2) at lower altitudes of the dip equator with sufficient field-line-integrated magnitudes.

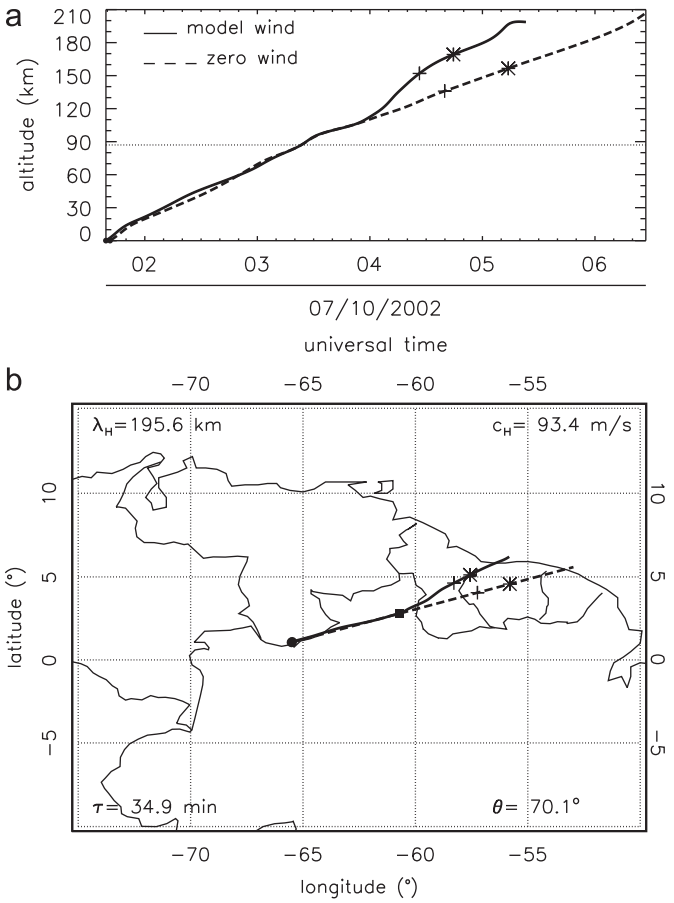

Fig. 5. Ray-tracing results for the MSGW observed on 28–29 October 2002. This event attained the highest altitude in the thermosphere–ionosphere. On top is shown the vertical ray path and on bottom is shown the horizontal ray path for a MSGW # 14. The GW parameters are printed on corners.

Paulino et al. (2011) showed seven GWs with EPB spacings and horizontal wavelength very close each other (#1–4, #9, #11, and #14). Using MW, six of them (#1, #3, #4, #9, #11, and #14) were seen to propagate in the TI up to 120 km. Therefore, a direct action of these MSGWs in the RTI triggering seems unlikely. Only, one of them (#2) propagated up to high altitudes ($>$ 140 km). Off the magnetic equator, as Boa Vista is, a GW may influence RTI due to field-line-integrated effects if the GW had the phase structure aligned along the slanted magnetic field line (e.g., Prakash and Pandey, 1985; Fritts et al., 2008). It means that GWs propagating toward the magnetic equator may be more efficient as shown in the case of #5. Simulations of these GW effects on Spread-F initiation may give a better understanding of this coupling process, but this matter is out of the scope of this study. In summary, calculation of the MSGW paths in the TI showed that:

1. Most observed MSGWs were tilted toward the northwest direction and propagated longer horizontal distances in the presence of winds.
2. The ray-tracing results indicate that most of the Doppler up-shifted MSGWs in the MLT reached higher levels in the thermosphere than un-shifted ones.
3. Event #10 reached a high altitude in the TI (180–200 km), and had a large zonal amplitude of $\sim$19 m/s at the maximum momentum flux height. Therefore, this event could be a candidate for directly triggering the RTI instability.
4. Two-third of the MSGWs observed during the COPEX campaign propagated up to 150 km heights. Among them, three cases did show further upward propagation above 150 km altitude.
5. Study of GW effects on seeding RTI may be more efficient by using airglow imaging if the GWs propagate westward.

Acknowledgments

The authors are grateful to José Augusto de Souza for the technical support during the COPEX Campaign. The imager used during COPEX at Boa Vista was financed by CNPq/PRONEX Grant No. 76.97.1079.00. This work has also been supported by the Fundação de Amparo a Pesquisa do Estado de São Paulo (2011/20120-5). C.M. Wrasse thanks CNPq for the Grant 304277/2008-8. S.L. Vadas was supported by NSF Grant ATM-0836195. The authors appreciate the efforts of the Community Coordinated Modeling Center and High Altitude Observatory to make available on-line the NRLMSISE-00, HWM-93 and HWM-07, and TIE-GCM models, respectively.

References

Abdu, M.A., Alam Kherani, E., Batista, I.S., de Paula, E.R., Fritts, D.C., Sobral, J.H.A., 2009a. Gravity wave initiation of equatorial spread F/plasma bubble irregularities based on observational data from the SpreadFEx campaign. Annales de Geophysique 27, 2607–2622, aNGEO 0992-7689.

Abdu, M.A., Batista, I.S., Reinisch, B.W., de Souza, J.R., Sobral, J.H.A., Pedersen, T.R., Medeiros, A.F., Schuch, N.J., de Paula, E.R., Groves, K.M., 2009b. Conjugate Point Equatorial Experiment (COPEX) campaign in Brazil: electrodynamics highlights on spreadFdevelopment conditions and day-to-day variability. Journal of Geophysical Research (Space Physics) 114, 04308, http://dx.doi.org/10.1029/2008JA013749.

Anderson, D.N., Richmond, A.D., Balsley, B.B., Roble, R.G., Biondi, M.A., Sipler, D.P., 1982. In-situ generated gravity waves as a possible seeding mechanism for equatorial spread-F. Geophysical Research Letters 9, 789–792, http://dx.doi.org/10.1029/GL009i007p00789.

Dewan, E.M., Picard, R.H., O'Neil, R.R., Gardiner, H.A., Gibson, J., Mill, J.D., Richards, E., Kendra, M., Gallery, W.O., 1998. MSX satellite observations of thunderstorm-generated gravity waves in mid-wave infrared images of the upper stratosphere. Geophysical Research Letters 25, 939–942 0094-8276.

Drob, D.P., Emmert, J.T., Crowley, G., Picone, J.M., Shepherd, G.G., Skinner, W., Hays, P., Niciejewski, R.J., Larsen, M., She, C.Y., Meriwether, J.W., Hernandez, G., Jarvis, M.J., Sipler, D.P., Tepley, C.A., O'Brien, M.S., Bowman, J.R., Wu, Q., Murayama, Y., Kawamura, S., Reid, I.M., Vincent, R.A., 2008. An empirical model of the Earth's horizontal wind fields: HWM07. Journal of Geophysical Research (Space Physics) 113, 12304. http://dx.doi.org/10.1029/2008JA013668.

Fritts, D.C., Alexander, M.J., 2003. Gravity wave dynamics and effects in the middle atmosphere. Reviews of Geophysics 41, 1003, http://dx.doi.org/10.1029/2001RG000106.

Fritts, D.C., Vadas, S.L., 2008. Gravity wave penetration into the thermosphere: sensitivity to solar cycle variations and mean winds. Annales de Geophysique 26, 3841–3861, aNGEO 0992-7689.

Fritts, D.C., Vadas, S.L., Riggin, D.M., Abdu, M.A., Batista, I.S., Takahashi, H., Medeiros, A., Kamalabadi, F., Liu, H.L., Fejer, B.G., Taylor, M.J., 2008. Gravity wave and tidal influences on equatorial spread F based on observations during the Spread F Experiment (SpreadFEx). Annales de Geophysique 26, 3235–3252, aNGEO 0992-7689.

Fritts, D.C., Abdu, M.A., Batista, B.R., Batista, I.S., Batista, P.P., Buriti, R., Clemesha, B.R., Dautermann, T., de Paula, E.R., Fechine, B.J., Fejer, B.G., Gobbi, D., Haase, J., Kamalabadi, F., Kherani, E.A., Laughman, B., Lima, P.P., Liu, H.L., Medeiros, A., Pautet, P.D., Riggin, D.M., Rodrigues, F.S., São Sabbas, F., Sobral, J.H.A., Stamus, P., Takahashi, H., Taylor, M.J., Vadas, S.L., Vargas, F., Wrasse, C.M., 2009. Overview and summary of the Spread F Experiment (SpreadFEx). Annales de Geophysique 27, 2141–2155, aNGEO 0992-7689.

Hedin, A.E., Fleming, E.L., Manson, A.H., Schmidlin, F.J., Avery, S.K., Clark, R.R., Franke, S.J., Fraser, G.J., Tsuda, T., Vial, F., Vincent, R.A., 1996. Empirical wind model for the upper, middle and lower atmosphere, Journal of Atmospheric and Terrestrial Physics 58, 1421(1447, 0021–9169 http://dx.doi.org/10.1016/0021-9169(95)00122-0).

Huang, C.-S., Kelley, M.C., 1996. Nonlinear evolution of equatorial spread F 2. Gravity waves seeding of Rayleigh–Taylor instability. Journal of Geophysical Research 101, 293–302.

Huang, C.-S., Kelley, M.C., Hysell, D.L., 1993. Nonlinear Rayleigh–Taylor instabilities, atmospheric gravity waves and equatorial spread F. Journal of Geophysical Research 98, 15631–15642.

Hysell, D.L., Kelley, M.C., Swartz, W.E., Woodman, R.F., 1990. Seeding and layering of equatorial spread F by gravity waves. Journal of Geophysical Research 95, 17253–17260, http://dx.doi.org/10.1029/JA095iA10p17253.

Kelley, M.C., Larsen, M.F., LaHoz, C., 1981. Gravity wave initiation of equatorial spread F: a case study. Journal of Geophysical Research 86, 9087–9100.
Keskinen, M.J., Vadas, S.L., 2009. Three-dimensional nonlinear evolution of equatorial ionospheric bubbles with gravity wave seeding and tidal wind effects. Geophysical Research Letters 36, 12102, http://dx.doi.org/10.1029/2009GL037892.
Kherani, A.E., Abdu, M.A., de Paula, E.R., Fritts, D.C., Sobral, J.H.A., de Meneses Jr., F.C., 2009. The impact of gravity waves rising from convection in the lower atmosphere on the generation and nonlinear evolution of equatorial bubble. Annales de Geophysique 27, 1657–1668, aNGEO 0992-7689.
Kudeki, E., Bhattacharyya, S., 1999. Postsunset vortex in equatorial F-region plasma drifts and implications for bottomside spread-F. Journal of Geophysical Research 104, 28163–28170, http://dx.doi.org/10.1029/1998JA900111.
Kudeki, E., Akgiray, A., Milla, M., Chau, J.L., Hysell, D.L., 2007. Equatorial spread-F initiation: Post-sunset vortex, thermospheric winds, gravity waves. Journal of Atmospheric and Solar-Terrestrial Physics 69, 2416–2427.
Lighthill, J., 1978. Waves in Fluids. Cambridge University Press, New York.
Makela, J.J., Vadas, S.L., Muryanto, R., Duly, T., Crowley, G., 2010. Periodic spacing between consecutive equatorial plasma bubbles. Geophysical Research Letters 37, L14103 0094-8276.
Marks, C.J., Eckermann, S.D., 1995. A three-dimensional nonhydrostatic ray-tracing model for gravity waves: formulation and preliminary results for the middle atmosphere. Journal of the Atmospheric Sciences 52, 1959–1984.
McClure, J.P., Singh, S., Bamgboye, D.K., Johnson, F.S., Kil, H., 1998. Occurrence of equatorial F region irregularities: evidence for tropospheric seeding. Journal of Geophysical Research 103, 29119–29136, http://dx.doi.org/10.1029/98JA02749.
Miyoshi, Y., Fujiwara, H., 2008. Gravity waves in the thermosphere simulated by a general circulation model. Journal of Geophysical Research 113, D01101 0148-0227.
Paulino, I., Takahashi, H., Medeiros, A.F., Wrasse, C.M., Buriti, R.A., Sobral, J.H.A., Gobbi, D., 2011. Mesospheric gravity waves and ionospheric plasma bubbles observed during the COPEX campaign. Journal of Atmospheric and Solar-Terrestrial Physics 73, 1575–1580, http://dx.doi.org/10.1016/j.jastp.2010.12.004 1364-6826.
Pfister, L., Chan, K.R., Bui, T.P., Bowen, S., Legg, M., Gary, B., Kelly, K., Proffitt, M., Starr, W., 1993. Gravity waves generated by a tropical cyclone during the STEP tropical field program: a case study. Journal of Geophysical Research 98, 8611–8638.
Picone, J.M., Hedin, A.E., Drob, D.P., Aikin, A.C., 2002. NRLMSISE-00 empirical model of the atmosphere: statistical comparisons and scientific issues. Journal of Geophysical Research 107, 1468 0148-0227.
Prakash, S., Pandey, R., 1985. Generation of electric fields due to the gravity wave winds and their transmission to other ionospheric regions. Journal of Atmospheric and Terrestrial Physics 47, 363–374.
Richmond, A.D., 1978. Gravity wave generation, propagation, and dissipation in the thermosphere. Journal of Geophysical Research 83, 4131–4145, http://dx.doi.org/10.1029/JA083iA09p04131.
Roble, R.G., Ridley, E.C., 1994. A thermosphere–ionosphere–mesosphere-electrodynamics general circulation model (time-GCM): equinox solar cycle minimum simulations (30–500 km). Geophysical Research Letters 21, 417–420 0094-8276.
Rottger, J., 1982. Gravity waves seeding ionospheric irregularities. Nature 296, 111, http://dx.doi.org/10.1038/296111a0, aAA ID. AAA031.083.004.
Sentman, D.D., Wescott, E.M., Picard, R.H., Winick, J.R., Stenbaek Nielsen, H.C., Dewan, E.M., Moudry, D.R., São Sabbas, F.T., Heavner, M.J., Morrill, J., 2003. Simultaneous observations of mesospheric gravity waves and sprites generated by a midwestern thunderstorm. Journal of Atmospheric and Solar-Terrestrial Physics 65, 537–550, http://dx.doi.org/10.1016/S1364-6826(02)00328-0 1364-6826.
Sobral, J.H.A., Abdu, M.A., Batista, I.S., Zamlutti, C.J., 1981. Wave disturbances in the low latitude ionosphere and equatorial ionospheric plasma depletions. Journal of Geophysical Research 86, 1374–1378 0148-0227.
Sobral, J.H.A., Takahashi, H., Abdu, M.A., Taylor, M.J., Sawant, H., Santana, D.C., Gobbi, D., de Medeiros, A.F., Zamlutti, C.J., Schuch, N.J., Borba, G.L., 2001. Thermospheric F-region travelling disturbances detected at low latitude by an OI 630 nm digital imager system. Advances in Space Research 27, 1201–1206.
Sobral, J.H.A., Abdu, M.A., Pedersen, T.R., Castilho, V.M., Arruda, D.C.S., Muella, M.T.A.H., Batista, I.S., Mascarenhas, M., de Paula, E.R., Kintner, P.M., Kherani, E.A., Medeiros, A.F., Buriti, R.A., Takahashi, H., Schuch, N.J., Denardini, C.M., Zamlutti, C.J., Pimenta, A.A., de Souza, J.R., Bertoni, F.C.P., 2009. Ionospheric zonal velocities at conjugate points over Brazil during the COPEX campaign: experimental observations and theoretical validations. Journal of Geophysical Research (Space Physics) 114, 04309, http://dx.doi.org/10.1029/2008JA013896.
Sultan, P.J., 1996. Linear theory and modeling of the Rayleigh–Taylor instability leading to the occurrence of equatorial spread F. Journal of Geophysical Research 101, 26875–26892, http://dx.doi.org/10.1029/96JA00682.
Suzuki, S., Shiokawa, K., Otsuka, Y., Ogawa, T., Nakamura, K., Nakamura, T., 2007. A concentric gravity wave structure in the mesospheric airglow images. Journal of Geophysical Research 112, D02102 0148-0227.
Takahashi, H., Taylor, M.J., Pautet, P.D., Medeiros, A.F., Gobbi, D., Wrasse, C.M., Fechine, J., Abdu, M.A., Batista, I.S., Paula, E., Sobral, J.H.A., Arruda, D., Vadas, S.L., Sabbas, F.S., Fritts, D.C., 2009. Simultaneous observation of ionospheric plasma bubbles and mesospheric gravity waves during the SpreadFEx Campaign. Annales de Geophysique 27, 1477–1487, aNGEO 0992-7689.
Takahashi, H., Abdu, M.A., Taylor, M.J., Pautet, P.D., de Paula, E., Kherani, E.A., Medeiros, A.F., Wrasse, C.M., Batista, I.S., Sobral, J.H.A., Gobbi, D., Arruda, D., Paulino, I., Vadas, S., Fritts, D., 2010. Equatorial ionosphere bottom-type spread F observed by OI 630.0 nm airglow imaging. Geophysical Research Letters 37.
Takahashi, H., Vadas, S.L., Wrasse, C.M., Taylor, M.J., Pautet, P.D., Medeiros, A.F., Buriti, R.A., Paula, E.R., Abdu, M.A., Batista, I.S., Paulino, I., Stamus, P.A., Fritts, D.C., 2011. Mesosphere–ionosphere coupling processes observed in the F layer bottom-side oscillation. In: Hultqvist, B. (Ed.), Aeronomy of the Earth's Atmosphere and Ionosphere, IAGA Special Sopron Book Series, vol. 2. Springer Netherlands, pp. 163–175 978-94-007-0326-1.
Taylor, M.J., Jahn, J.M., Fukao, S., Saito, A., 1998. Possible evidence of gravity wave coupling into the mid-latitude F region ionosphere during the SEEK campaign. Geophysical Research Letters 25, 1801–1804, http://dx.doi.org/10.1029/97GL03448.
Tsunoda, R.T., 2007. Seeding of equatorial plasma bubbles with electric fields from an Es-layer instability. Journal of Geophysical Research (Space Physics) 112, 06304, http://dx.doi.org/10.1029/2006JA012103.
Tsunoda, R.T., 2010. On seeding equatorial spread F: circular gravity waves. Geophysical Research Letters 37, L10104 0094-8276.
Vadas, S.L., 2007. Horizontal and vertical propagation and dissipation of gravity waves in the thermosphere from lower atmospheric and thermospheric sources. Journal of Geophysical Research (Space Physics) 112, 06305, http://dx.doi.org/10.1029/2006JA011845.
Vadas, S.L., Fritts, D.C., 2005. Thermospheric responses to gravity waves: influences of increasing viscosity and thermal diffusivity. Journal of Geophysical Research (Atmospheres) 110, 15103, http://dx.doi.org/10.1029/2004JD005574.
Vadas, S.L., Fritts, D.C., 2009. Reconstruction of the gravity wave field from convective plumes via ray tracing. Annales de Geophysique 27, 147–177, aNGEO 0992-7689.
Vadas, S.L., Liu, H.-l., 2009. Generation of large-scale gravity waves and neutral winds in the thermosphere from the dissipation of convectively generated gravity waves. Journal of Geophysical Research 114, A10310 0148-0227.
Vadas, S.L., Liu, H.-L., 2011. Neutral Winds and Densities at the Bottomside of the F Layer from Primary and Secondary Gravity Waves from Deep Convection Aeronomy of the Earth's Atmosphere and Ionosphere, IAGA Special Sopron Book Series, vol. 2. Springer, Netherlands, pp. 131–139, 978-94-007-0326-1.
Vadas, S.L., Nicolls, M.J., 2008. Using PFISR measurements and gravity wave dissipative theory to determine the neutral, background thermospheric winds. Geophysical Research Letters 35, 02105, http://dx.doi.org/10.1029/2007GL031522.
Vadas, S.L., Nicolls, M.J., 2009. Temporal evolution of neutral, thermospheric winds and plasma response using PFISR measurements of gravity waves. Journal of Atmospheric and Solar-Terrestrial Physics 71, 744–770, http://dx.doi.org/10.1016/j.jastp.2009.01.011 1364-6826.
Vadas, S.L., Taylor, M.J., Pautet, P.D., Stamus, P.A., Fritts, D.C., Liu, H.L., São Sabbas, F.T., Rampinelli, V.T., Batista, P., Takahashi, H., 2009. Convection: the likely source of the medium-scale gravity waves observed in the OH airglow layer near Brasilia, Brazil, during the SpreadFEx campaign. Annales de Geophysique 27, 231–259, aNGEO 0992-7689.
Vargas, F., Gobbi, D., Takahashi, H., Lima, L.M., 2009. Gravity wave amplitudes and momentum fluxes inferred from OH airglow intensities and meteor radar winds during SpreadFEx. Annales de Geophysique 27, 2361–2369, aNGEO 0992-7689.
Yigit, E., Medvedev, A.S., 2010. Internal gravity waves in the thermosphere during low and high solar activity: simulation study. Journal of Geophysical Research 115, A00G02 0148-0227.
Yigit, E., Medvedev, A.S., Aylward, A.D., Hartogh, P., Harris, M.J., 2009. Modeling the effects of gravity wave momentum deposition on the general circulation above the turbopause. Journal of Geophysical Research 114, D07101 0148-0227.